

Original Research Article

Mapping of Hydrothermal Alteration Minerals Related to Tongue Tonguey (Sirba, Niger) Gold Mineralization Using Landsat 8 OLI data and Remote Sensing

ABSTRACT

Remote sensing is an effective means of exploring for gold resources. One of Niger's main gold provinces is the Sirba greenstone belt. Gold mineralization in the Tongue Tonguey soils presents interesting anomalies. It was necessary to identify and map the associated hydrothermal alteration. The aim of this work was to map hydrothermal alteration anomalies associated with gold mineralization. Band ratio technique was applied to Landsat 8 OLI data of the study area to highlight surfaces rich in alteration minerals. Band ratios (4/2) and (6/7) were applied to highlight iron minerals (hematite, goethite, jarosite) and alunite/clay minerals (kaolinite, montmorillonite, illite) respectively. Gold anomalies and alteration mineral anomalies were extracted from raster images using the threshold method. Iron minerals and alunite/clay minerals alterations were well associated with the gold anomalies host rocks. Hydrothermal alteration anomalies superimposed effectively on the gold anomalies. They were located in meta-volcano-sediments, along regional faults and at lithological contacts. Gold anomaly zones where iron minerals and alunite/clay minerals alterations was developed constitute favorable zones for gold exploration at Tongue Tonguey.

Keywords: Remote sensing, alteration anomalies, band ratios, Tongue Tonguey.

1. INTRODUCTION

Mineral exploration uses several prospecting methods such as geochemistry, geophysics, geological mapping, remote sensing and ground surveys to determine anomalies associated with mineralization (Daoud et al., 2025; Ibrahim et al., 2021). Remote sensing technology is more cost-effective for geological applications due to its low cost (Daoud et al., 2025). This technique involves the acquisition, processing and interpretation of images and related data acquired from aircraft and satellites that measure the interaction between the earth's surface features and electromagnetic energy (Gabr et al., 2010; Massironi et al., 2008; Pour and Hashim, 2011). Remote sensing applications in mineral exploration focus on the geological and structural mapping that controls the emplacement of mineralization and the recognition of hydrothermal

alteration of rocks by their spectral signatures (Rajesh, 2004). The presence of altered rocks is the main indicator of the presence of a probable ore deposit (Ibrahim et al., 2021). Remote sensing techniques had been widely used for mapping geological structures, discriminating lithologies and hydrothermal alterations, and for mineral exploration (Kujjo et al., 2018). Remote sensing reconnaissance of host rocks had been widely used for the exploration of gold and porphyry copper deposits (Azhar, 2023; Bedini, 2022; Bedini and Chen, 2020, Ibrahim et al., 2021). Although gold cannot be detected directly by remote sensing, the presence of minerals such as iron oxides and clay minerals could serve as hydrothermal alteration zones associated with gold occurrences (Kujjo, 2010). Rock spectra depend on the spectra of the constituent minerals and their textural properties, such as grain size, matrix and association (Sgavetti et al., 2006). In areas where bedrock was exposed, multispectral remote sensing can be used to identify weathered rocks because their reflectance spectra differ from those of unweathered bedrock (Sabins, 1999). Alteration zones are important guides to mineral exploration and are generally characterized by abundant minerals such as kaolinite, alunite, muscovite, chlorite, epidote, calcite, goethite, hematite, jarosite, etc (Pour and Hashim, 2015). Many mines had been discovered by recognizing outcrops of altered rock, the best indicators of which were iron oxides (Sabins, 1999) and hydrothermal clays (Poormirzaee and Oskouei, 2010). The Landsat 8 satellite uses the "Operational Land Imager (OLI)" sensor which enables to map clay minerals, alunite and secondary iron minerals associated with gold mineralization (Abass-Saley et al., 2021; Kujjo, 2010).

Numerous techniques had been developed to enhance image quality and highlight target minerals (Aliyu and Aliyu, 2020; Kamau et al., 2020; Osinowo et al., 2021; Sheikhrhimi et al., 2019). One of these techniques was the Band ratio, which was commonly used for mineral and lithological mapping (Azhar, 2023). The Band ratio helps to distinguish the lithological units (Ibrahim et al., 2021) and to extract information on hydrothermal alteration zones (Mars and Rowan, 2006). Band ratios had been widely used in mineral exploration to map alteration zones and their associated minerals (Khidir et Babikir, 2013; Kujjo et al., 2018).

The Sirba greenstone belt in which the study area is located was Niger's main gold province. Gold was mined both industrially and artisanally in the Sirba. Gold panning was the main non-agricultural activity in the region. The search for gold in this region had always been carried out using geological, geochemical and geophysical methods. The potential of remote sensing in the search for gold mineralization had not been tested. The various geological mapping and geophysical surveys carried out by the Ministry of Mines and various mining companies (Jica, 1995; Saint-Martin, 1999) had highlighted certain geological features (lithology, fracturing, etc.) favorable for the development of gold mineralization in the Sirba. In addition to the presence of several gold showings and deposits, and base metals discovered by the various geochemical prospecting campaigns, the work highlighted the presence of significant hydrothermal alteration and shear zones. These factors convinced us of the Sirba Trench's suitability for gold exploration, and of the need to undertake this work. The advent of GIS (Geographic Information System) platforms led to the development of a number of approaches for processing and combining multiple geological parameters in order to define areas suitable for the exploration of economic substances (Eteh et al., 2021). It is in this context that this work aims to map the alteration mineral anomalies related to Tongue Tonguey gold mineralization using Landsat 8 imagery.

2. GEOLOGICAL CONTEXT OF THE STUDY AREA

The Tongue Tonguey gold zone is located on the Sirba greenstone belt in Niger's Liptako. The latter corresponds to the NE end of the Léo-Man ridge (Fig. 1a) on the West African craton (Machens, 1973). The Liptako geological formations (Fig. 1b) were Lower Proterozoic in age (Bessoles, 1977). They were formed by alternating greenstone belts and granitoids (Machens, 1967) with Neoproterozoic and Mio-Pliocene sediments (Dupuis et al., 1991; Machens, 1973; Pons et al., 1995). Greenstone belts consist of pyroxenite, amphibolite, chloritoschist, meta-basalt, meta-gabbro, meta-sediments, meta-volcano-sediments, meta-volcano-plutonites, tuffs and rhyolitic breccias (Ama Salah et al., 1996; Soumaila, 2000; Soumaila et al., 2004). The plutons were composed of granite, tonalite, trondhjemite and granodiorite (Soumaila, 2000), intersected by sills and basic dykes (Dupuis et al., 1991; Pons et al., 1995). Tongue Tonguey's geological formations consist of undifferentiated meta-volcano-sediments, acidic meta-sediments, enclaves of amphibolite, quartz diorite, granite, and locally amphibolitized basic volcano-plutonite, quartz diorite, meta-gabbro, dolerite dykes and quartz vein outcrops, locally overlain by lateritic Continental Terminal armour and Quaternary sand dunes (Fig. 1c).

Gold mineralization in the West African Craton was largely associated with greenstone belts (Augustin, 2011; Markwitz et al., 2016; Milési et al., 1989) with over 80% of the craton's gold reserves (Castaing et al., 2003). Most gold deposits were dominated by quartz veins in shear zones and disseminated sulphide types formed at the end of the Eburnian orogeny (Béziat et al., 2008; Markwitz et al., 2015). Gold mineralization in the Liptako was closely linked to major regional faults and to the nature of the rocks (Klockner, 1995). Two types of gold mineralization had been identified in Liptako (Jica, 1995; Saint-Martin, 1999): syn-sedimentary exhalative gold mineralization associated with graphitic clays (Jica, 1995; Saint-Martin, 1999) and quartz vein or stockwork gold mineralization controlled by fractures and faults (Jica, 1995; Klockner, 1995; Saint-Martin, 1999; St-Julien, 1992). Gold mineralization was also related to gabbro, quartz diorite and rhyolite dyke clusters (Saint-Martin, 1999). Minerals observed in quartz veins include silver-bearing native gold, pyrite,

arsenopyrite, sphalerite, galena, chalcopyrite, hematite, goethite (Jica, 1995; Klockner, 1995; Poulin et al., 1987; Saint-Martin, 1999). Gold mineralization in the Sirba greenstone belt occurs mostly in quartz veins in association with sulfides that had transformed into iron oxides in zones that had disintegrated or altered (Saint-Martin, 1999). The Tongue Tonguey gold mineralization, like that of the Sirba greenstone belt, was associated with sulfides (pyrite, pyrrhotite, arsenopyrite, chalcopyrite) and their alteration products (hematite, goethite, etc.) (Jica, 1995; Saint-Martin, 1999).

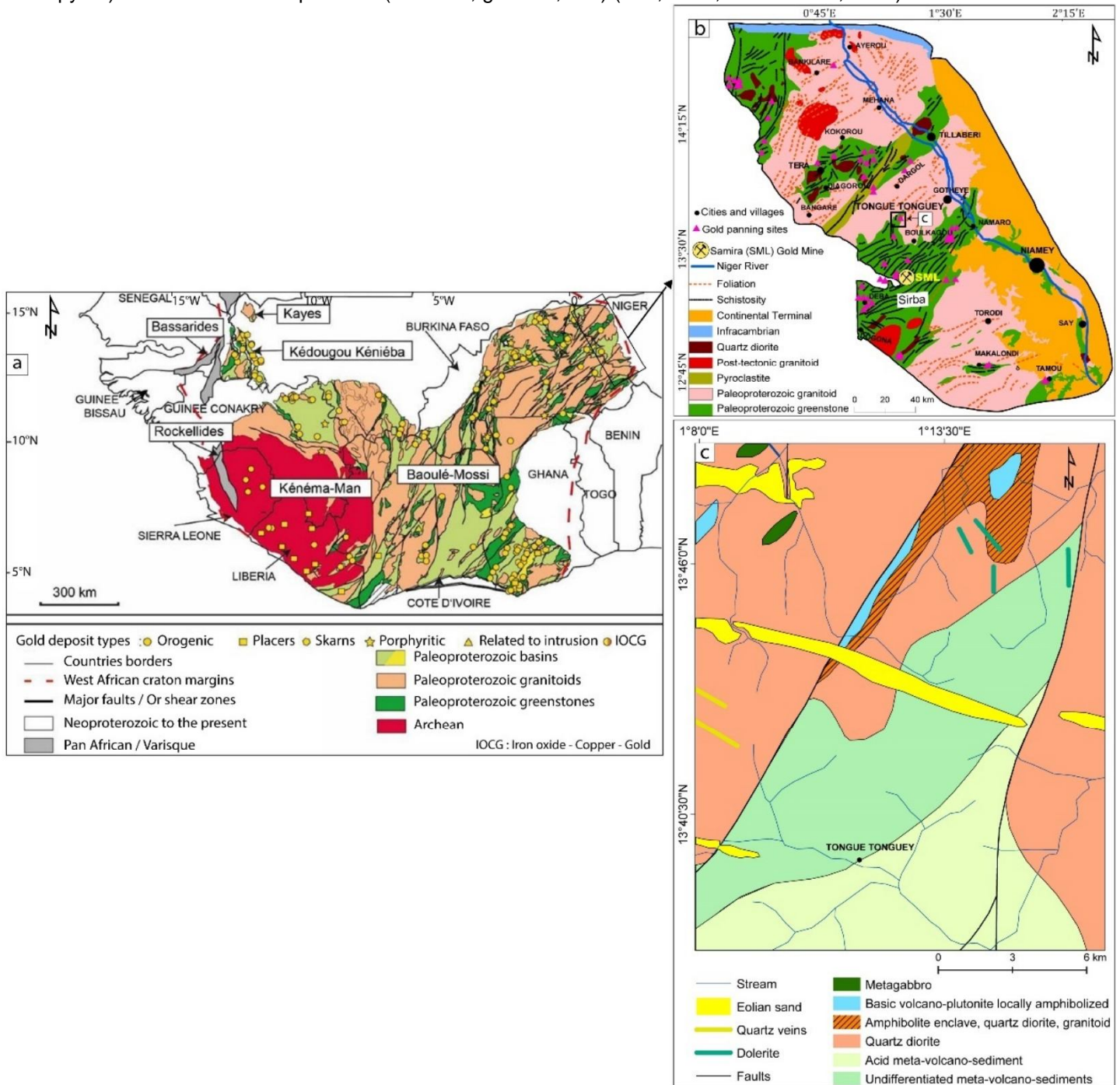


Fig. 1. Geological maps of the study area. a) Geological map of the Léo-Man Ridge (Milési et al., 2004) and location of gold deposits (Markwitz et al., 2016); b) Geological map of Liptako (Machens, 1967); c) Geological map of Tongue Tonguey (Abdou et al., 1997, modified).

3. DATA AND METHODOLOGY

Two types of data were used in this work: gold chemical analysis data from soil samples and Landsat 8 imagery of the study area.

The soil geochemistry data in this study come from the detailed geochemical prospecting campaign in the Sirba belt (1996-1997). Analytical results from 1,399 Tongue Tonguey soil samples were used. Gold analysis was performed by Chemex Labs Ltd. North Vancouver, B.C, Canada. The FA-NAA (Fire Assay Neutronic Atomic Absorption) method was used to determine the gold content of the soil samples after melting 10 g of sample. Fig. 2 shows the location of the soil sampling points (on the geological map).

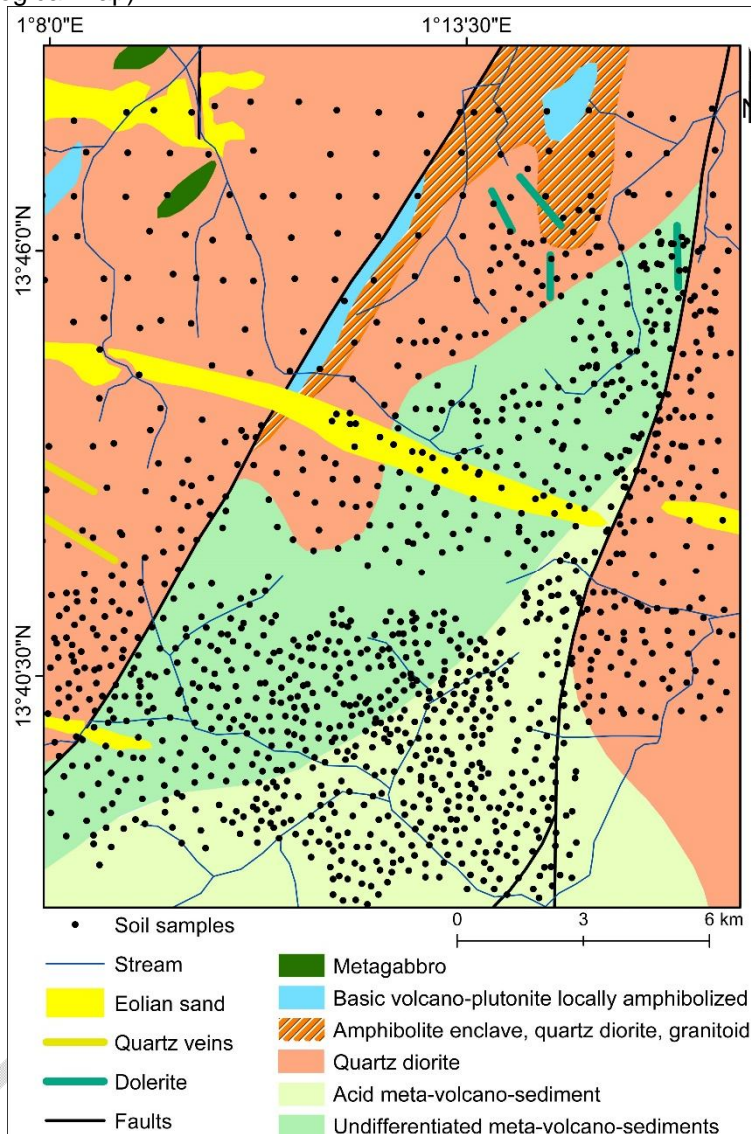


Fig. 2. Map of Tongue Tonguey soil sample points on the geological features.

A cloud-free level 1T (terrain-corrected) Landsat-8 image LC81930512018060LGN00 (path/row193/051) of the Tongue Tonguey area, acquired on March 01, 2018 was obtained from the USGS Earth Resources Observation and Science Center (<http://earthexplorer.usgs.gov>). Band designations, wavelengths and pixel sizes of the Landsat 8 imagery were given in Table 1, extracted from <https://www.usgs.gov/landsat-missions/landsat-8>.

Table 1. Characteristics of the Landsat 8 OLI/TIRS bands.

Spectral Band	Band Name	Wavelength (μm)	Spatial Resolution (m)
Coastal/ aerosol	Band 1	0.435 – 0.451	30
Blue	Band 2	0.452 – 0.512	30
Green	Band 3	0.533 – 0.590	30
Red	Band 4	0.636 – 0.673	30
NIR	Band 5	0.851 – 0.879	30
SWIR 1	Band 6	1.566 – 1.651	30
SWIR 2	Band 7	2.107 – 2.294	30

Pan	Band 8	0.503 – 0.676	15
Cirrus	Band 9	1.363 – 1.384	30
TIR	Band 10	10.60 – 11.19	100
TIR	Band 11	11.50 – 12.51	100

NIR: Near Infrared; SWIR: Short-Wave Infrared; TIR: Thermal Infrared; Pan: Panchromatic

3.1 Preprocessing of Landsat 8 data

The preprocessing operations applied to the Landsat 8 image consisted of radiometric calibration, atmospheric correction, conversion of radiometric values to reflectance (Han and Nelson, 2014; Labdaoui et al., 2023) and extraction of the study area image. After this step, the MNF (Minimum Noise Fraction) transformation was applied to the study area image to reduce the noise in the image (Dabiri and Lang, 2018; Shawky et al., 2019).

3.2 Spectral Band ratio

Band ratios improve spectral differences between bands and reduce the effects of topography (Sekandari et al., 2020). The ratio between two bands was calculated for each pixel digital number (DN values) in one spectral band were divided by the corresponding values in another band (Ali and Pour, 2014; Ghrefat et al., 2023). The resulting Band ratio image allows us to better distinguish hydrothermal alteration zones and lithological units (Abhary and Hassani, 2016; Frutuoso, 2015; Mwaniki et al., 2015; Ourhizif et al., 2019).

Iron minerals (hematite, goethite, jarosite) show similar spectral characteristics in the VNIR range due to their similar composition (Ge et al., 2020). They have low reflectance in the blue band (0.452-0.512 μm) and high reflectance in the red band (0.636-0.673 μm) (Table 1, Fig. 3a). Surfaces rich in these minerals will show high pixel values in an image with a Band 4 / Band 2 ratio (Kokaly et al., 2017; Pour et al., 2019; Traore et al., 2020).

Alunite and clay minerals (kaolinite, montmorillonite, illite) have a minimum reflectance in band 7 (2.107-2.294 μm) and a high reflectance in band 6 (1.566-1.651 μm) (Table 1, Fig. 3b). Landsat 8's Band ratio (6/7) highlights surfaces rich in clay minerals (kaolinite, illite, montmorillonite) and alunite through the presence of bright pixels (Kokaly et al., 2017; Pour et al., 2019; Pour and Hashim, 2015; Traore et al., 2020).

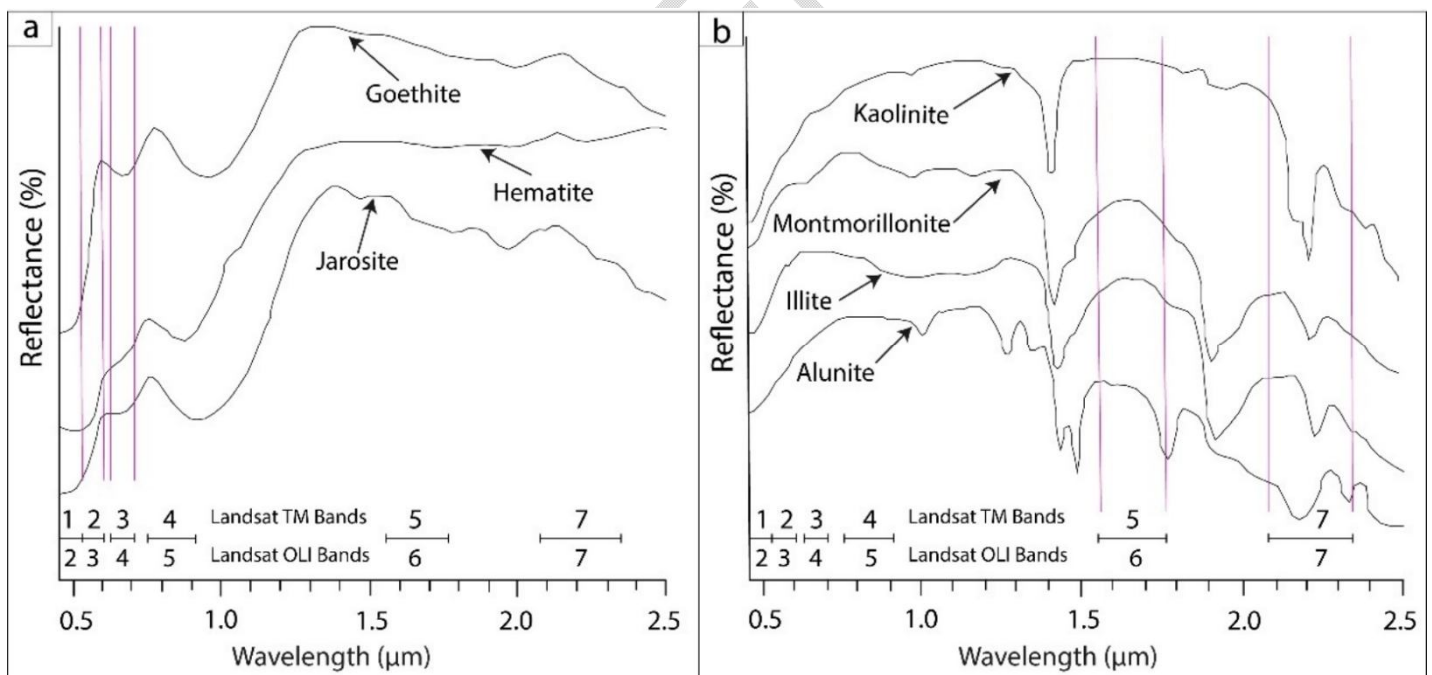


Fig. 3. Laboratory spectra of hematite and goethite, jarosite (a) and alunite, kaolinite, montmorillonite, illite (b) (Clark, 1999; Sabins, 1999) with approximate Landsat TM and OLI bands position.

3.3 Mapping of anomalies

Gold and alteration mineral anomalies were highlighted and extracted from raster images using Envi and ArcMap. The inverse distance weighted interpolation (IDW) method was applied to map gold concentrations. The interpolation map was converted to raster data with a 30 m spatial resolution. The image of gold anomalies and those resulting from band

ratios were recorded in grayscale (8 bits, 0 to 255). The threshold for each parameter was calculated from the DN values of each image (30 m spatial resolution) by applying one of the formulas (Elsaid, 2014):

$$\text{Threshold} = \text{Mean} + 3 * \text{Standard Deviation} \text{ (98\% of confidence)} \quad (1)$$

$$\text{Threshold} = \text{Mean} + 2 * \text{Standard Deviation} \text{ (95\% of confidence)} \quad (2)$$

4. RESULTS

4.1 Mapping of gold anomalies

The results deal first with the chemical analysis of gold. The statistical values of gold concentrations in Tongue Tonguey soil samples are shown in Table 2. Table 3 shows the statistical values of the raster image of the Tongue Tonguey gold anomalies. Fig. 4 shows the histogram and distribution curve of gold concentrations in Tongue Tonguey soil samples. Fig. 5 shows the spatial distribution of gold concentrations around mean and standard deviation values (Fig. 5a) and the map of Tongue Tonguey gold anomalies (Fig. 5b).

Table 2. Statistical values of gold concentrations (in ppb)

Element	Nt	Min	Mean	Stdev	Skewness	Max
Au	1399	0.5	85.78	403.70	24.33	13000

Nt: total number; Min: Minimum; Stdev: Standard deviation; Max: Maximum

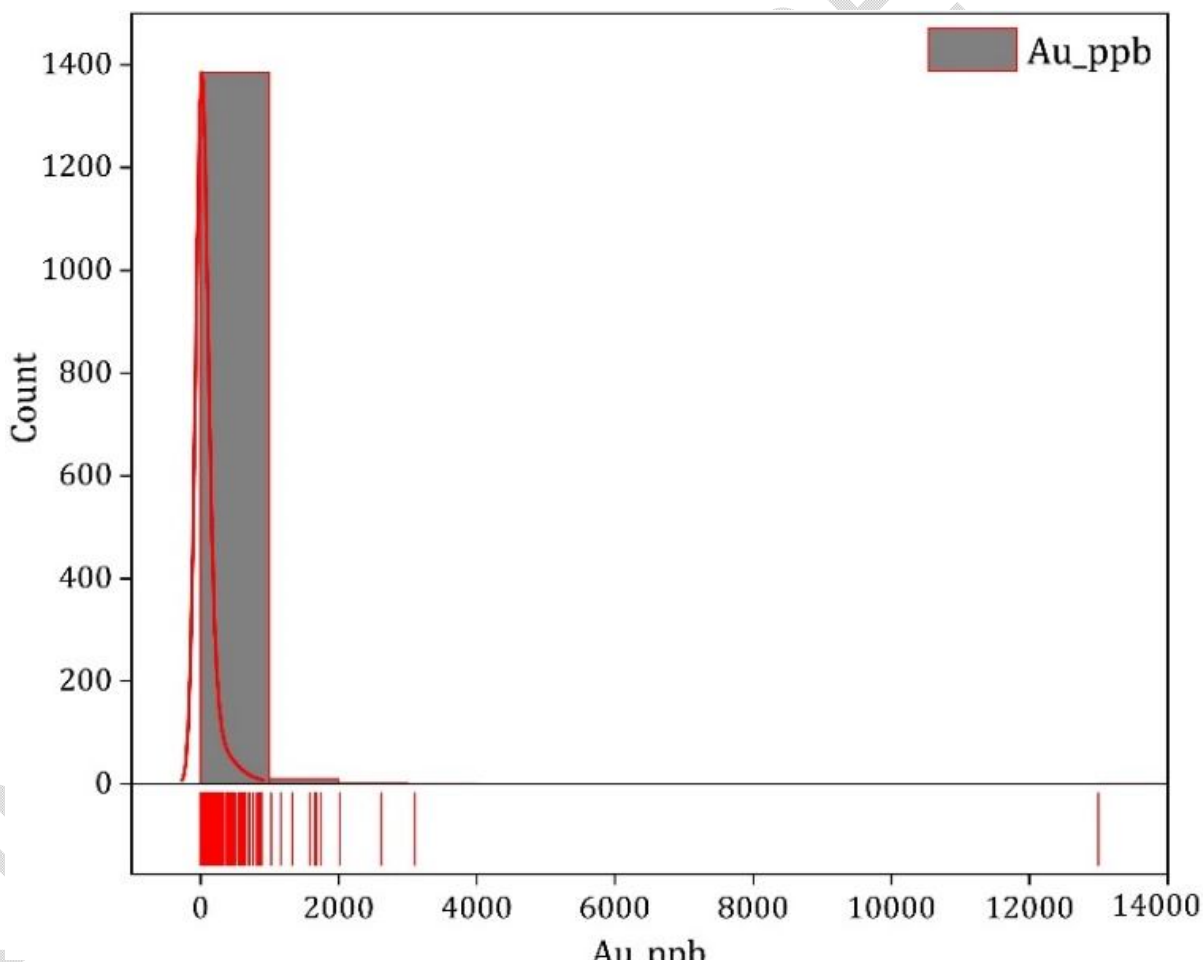


Fig. 4. Histogram and distribution curve of gold concentrations.

Table 3. Raster image statistics for the Tongue Tonguey gold anomalies

Anomaly	Min	Max	Mean	Stdev	Thd	Conf
Gold (Au)	0	255	31.39	56.84	145.07	95%

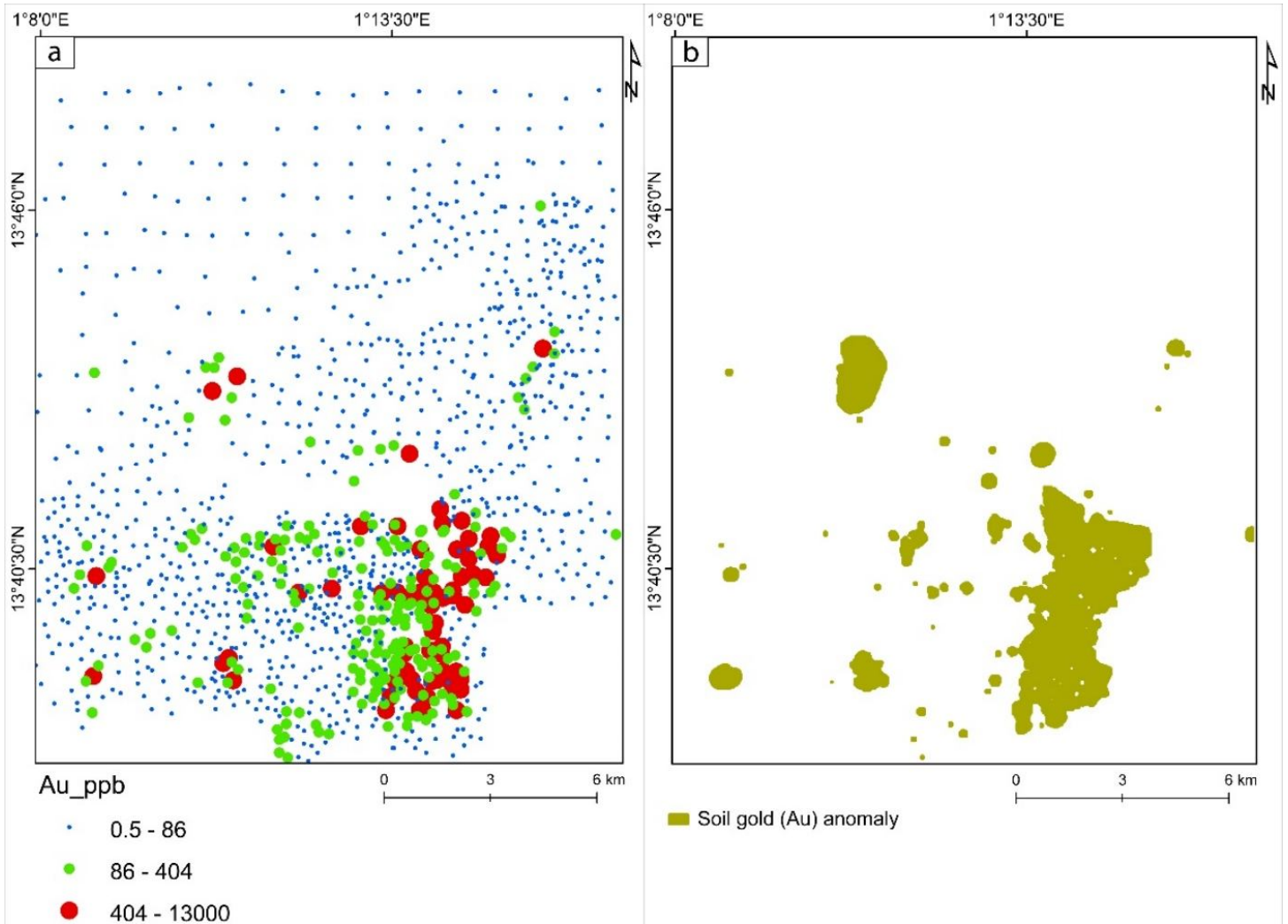


Fig. 5. Spatial distribution of gold at Tongue Tonguey. a) Spatial distribution of gold concentrations; b) Map of gold anomaly.

4.2 Mapping of hydrothermal mineral anomalies

Fig. 6 shows the Band ratio results for iron minerals (Fig. 6a) and for alunite and clay minerals (Fig. 6b). Areas in light pixels represent surfaces rich in iron minerals, clay minerals and alunite. Table 4 gives the statistics for iron minerals, alunite and clay minerals anomalies in the band ratio's raster images. Fig. 7 shows the spatial distribution of iron mineral anomalies (Fig. 7a) and alunite and clay mineral anomalies (Fig. 7b).

Fig. 8 shows the overlay of anomalies. Fig. 8a shows the overlay of iron mineral anomalies and alunite and clay mineral anomalies on the gold soil anomalies. Fig. 8b shows the superposition of iron mineral anomalies, alunite and clay mineral anomalies and gold soil anomalies on the Tongue Tonguey geological background.

Table 4. Raster image statistics of mineral anomalies from band ratios

Anomaly	Min	Max	Mean	Stdev	Thd	Conf
Iron minerals	0	255	117.75	63.41	244.56	95%
Alunite and Clay minerals	0	255	79.55	52.99	238.50	98%

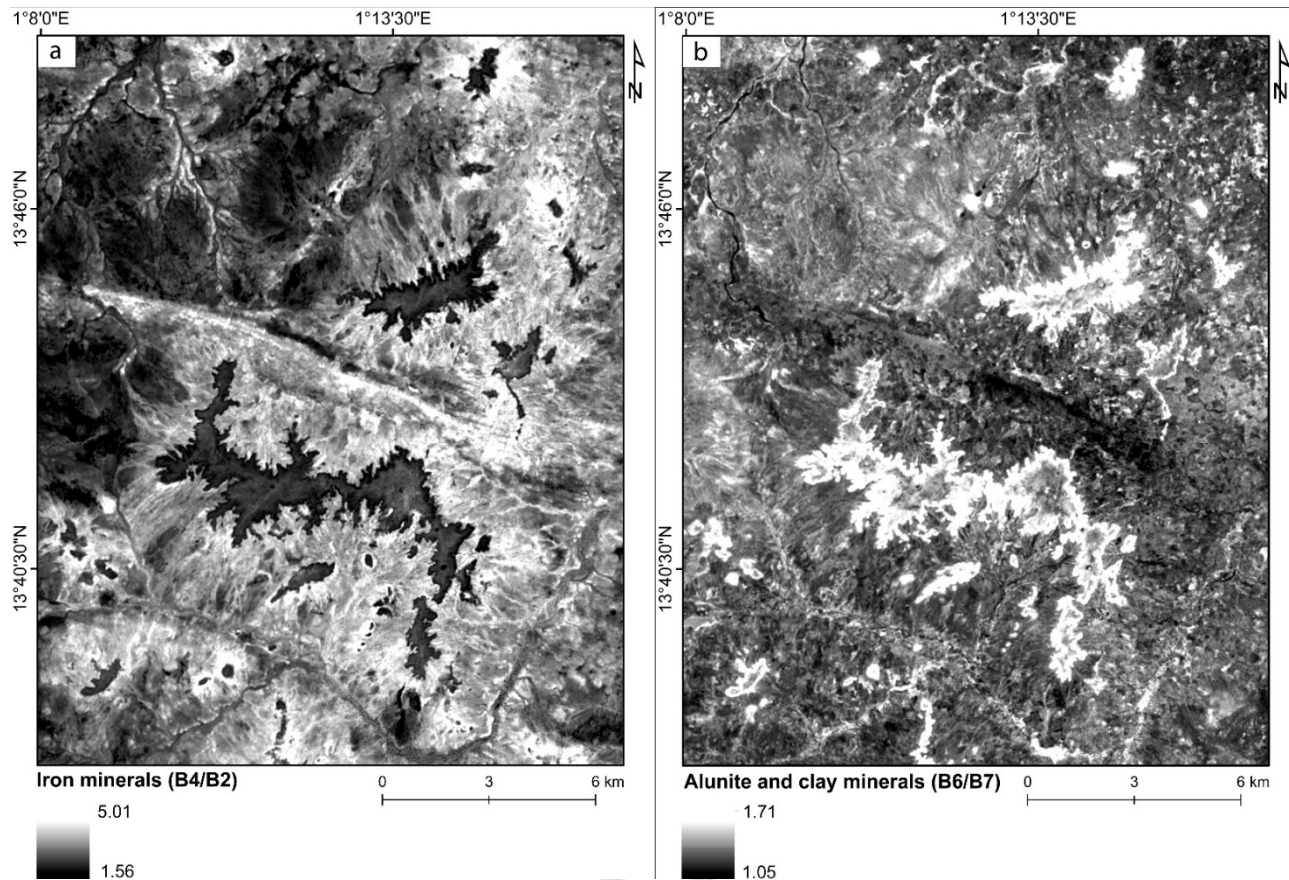


Fig. 6. Distribution maps of alteration minerals. a) Iron minerals; b) Alunite and clay minerals.

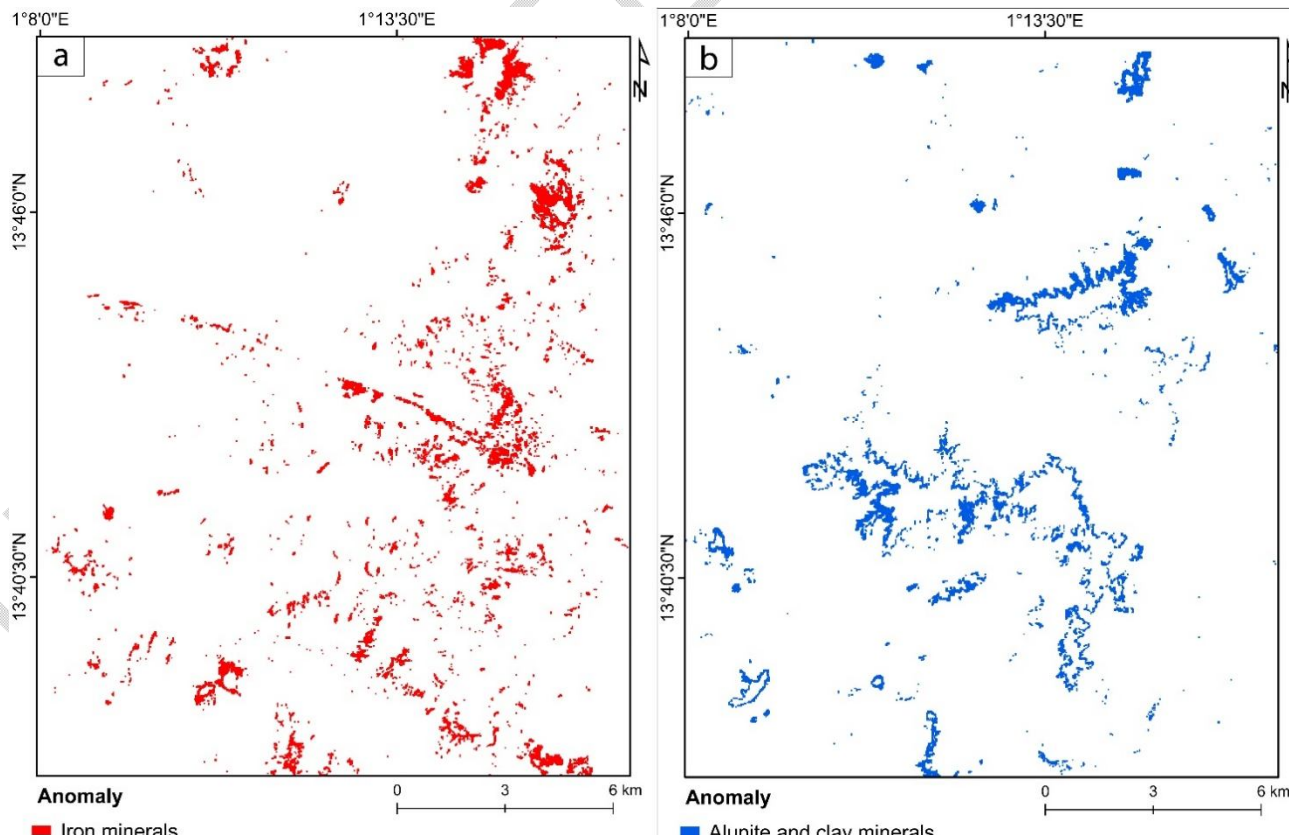


Fig. 7. Distribution of mineral anomalies. a) Iron minerals anomaly; b) Alunite and clay minerals anomaly.

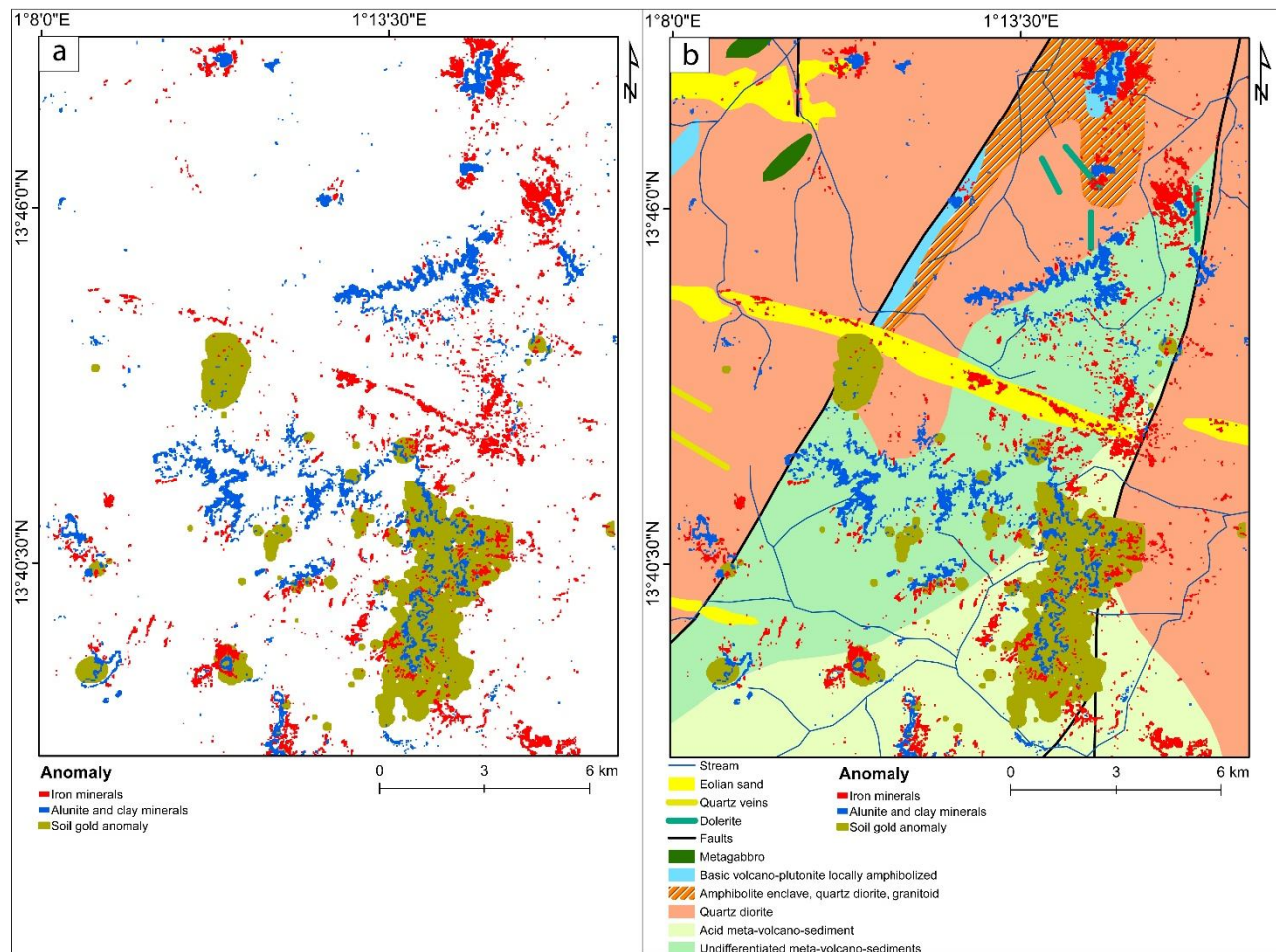


Fig. 8. Superposition of all anomalies. a) Superposition of hydrothermal minerals and gold anomalies; b) Superposition of hydrothermal minerals and gold anomalies on the area geological map.

5. DISCUSSION

Remote sensing satellite imagery had been successfully used to detect the hydrothermal alteration minerals associated with gold mineralization in metallogenic provinces (Boateng et al., 2018; Payamani et al., 2020; Sabins, 1999; Sheikhrhimi et al., 2019; Xu et al., 2019). In this investigation, spectral data derived from Landsat-8 sensor were used for detailed mapping hydrothermal alteration minerals in the Tongue Tonguey area, in the Sirba greenstone belt. Band ratios image processing technique was used to produce thematic maps of hydrothermal alteration minerals for indicating the high anomaly zones. Gold concentrations in Tongue Tonguey soils were very spread out (min = 0.5, max = 13,000, mean = 85.78) and highly skewed (skewness = 24.33). Most of the data were on the left, with a few extremely high values (outliers) on the right. The rocks hosting the Tongue Tonguey gold mineralization were subjected to hydrothermal alteration. The spatial distribution of alunite and clay minerals and iron minerals were mapped using the 6/7 and 4/2 band ratio of the Landsat-8 image. Gold anomalies were superimposed on hydrothermal alteration mineral anomalies (iron minerals, alunite and clay minerals). Iron mineral anomalies (hematite, goethite, jarosite) result from the alteration of iron sulfides. Iron sulfides (pyrite, arsenopyrite, pyrrhotite, chalcopyrite) characterized the gossan and the ore zone (Sabins, 1999). When these sulfides were exposed at the surface, they oxidize to form secondary iron minerals such as goethite, jarosite and hematite, as also reported by Sabins (1999). Long et al. (1992) showed that alunite and jarosite derived from aluminosilicates and pyrite. Kaolinite derived from plagioclase and montmorillonite derived from volcanic glass (Kruse and Hauff, 1990). Kaolinite and montmorillonite characterized the argillic alteration zone (Sabins, 1999). Hydrothermal alteration had developed preferentially on meta-volcano-sediments and basic rocks. Gold anomalies were observed on meta-volcano-sedimentary rocks, along regional faults and at lithological contacts. This observation was made throughout the Liptako region by Jica (1995), Klockner (1995) and Saint-Martin (1999). These gold anomalies may represent favorable zones for gold exploration due to the high intensity of silicates and sulfides alteration in the source rocks. In fact, Jica (1995) and Saint-Martin (1999) had shown that the Sirba greenstone gold mineralization was associated with sulfides such as pyrite, chalcopyrite and arsenopyrite, and iron oxides/hydroxides such as hematite and goethite.

6. CONCLUSION

The Tongue Tongue geological formations are dominated by meta-volcano-sediments and meta-sediments that had been subjected to intense hydrothermal alteration. The gold mineralization was associated to meta-volcano-sediments, regional faults and lithological contacts. The host rocks of the gold mineralization had been subjected to hydrothermal alteration. The application of the band ratio technique to Landsat 8 imagery highlighted iron minerals (hematite, goethite, jarosite), and alunite and clay minerals (kaolinite, montmorillonite, illite) alteration. Both types of alteration had developed on the meta-volcano-sediments, preferentially on the gold anomalies. Gold mineralization at Tongue Tongue was therefore characterized by iron minerals alteration and alunite/clay minerals alteration. These alteration minerals should constitute an excellent guide for gold exploration in the Tongue Tongue area.

DISCLAIMER (ARTIFICIAL INTELLIGENCE)

Author(s) hereby declare that NO generative AI technologies such as Large Language Models (ChatGPT, COPILOT, etc) and text-to-image generators have been used during writing or editing of this manuscript.

COMPETING INTERESTS

Authors have declared that no competing interests exist.

REFERENCES

1. Abass-Saley, A., Baratoux, D., Baratoux, L., Ahoussi, K.E., Yao, K.A., Kouamé, K.J. (2021). Evolution of the Koma Bangou Gold Panning Site (Niger) From 1984 to 2020 Using Landsat Imagery. *Earth Space Sci* 8, 25. <https://doi.org/10.1029/2021EA001879>
2. Abdou, A., Bonnot, H., Bory Kaldey, D., Chalamet, D., Saint Martin, M., Younfa, I. (1997). Explanatory notes for the Liptako geological maps 1/100000 and 1/200000. Ministry of Mines, Niger.
3. Abhary, A., Hassani, H. (2016). Mapping Hydrothermal Mineral Deposits Using PCA and BR Methods in Baft 1:100000 Geological Sheet, Iran. *IJAEMS* 2(9), 6.
4. Ali, A., Pour, A. (2014). Lithological mapping and hydrothermal alteration using Landsat 8 data: a case study in ariab mining district, red sea hills, Sudan. *International Journal of Basic and Applied Sciences* 3, 199–208. <https://doi.org/10.14419/ijbas.v3i3.2821>
5. Aliyu, O., Aliyu, K. (2020). Utilizing landsat-8 sensor operational land image data for hydrothermal alteration mapping within Anka Schist Belt, northwestern Nigeria. *Zb Depart geogr, turizam i hotel* 127–149. <https://doi.org/10.5937/ZbDght2002127A>
6. Ama Salah, I., Liegeois, J.-P., Pouclet, A. (1996). Evolution of an early Birimian oceanic island arc in the Niger Liptako (Sirba): geology, geochronology and geochemistry. *Journal of African Earth Sciences* 22, 235–254.
7. Augustin, J. (2011). Control factors and metallogenic processes of gold mineralization in the Wona deposit, Mana Mine, Burkina Faso. Master's degree in Earth Sciences, Université du Québec à Chicoutimi, 220p. <https://doi.org/10.1522/030174758>
8. Azhar, Kh.S.B. (2023). Discrimination different lithological units using a remote sensing application: A case study in the Dokan Area, Kurdistan Region–Iraq. *Journal of Water and Land Development*. <https://doi.org/10.24425/jwld.2022.142312>
9. Bedini, E. (2022). Investigation of quartz-alunite epithermal gold deposits using PRISMA satellite imagery: examples from Goldfield, Nevada, USA and Rodalquilar, Spain. *Jour. Hypers. Rem. Sensg.* 12, 216–224. <https://doi.org/10.29150/jhrs.v12.5.p216-224>
10. Bedini, E., Chen, J. (2020). Application of PRISMA satellite hyperspectral imagery to mineral alteration mapping at Cuprite, Nevada, USA. *Jour. Hypers. Rem. Sensg.* 10, 87–94. <https://doi.org/10.29150/jhrs.v10.2.p87-94>
11. Bessoles, B. (1977). *Geology of Africa: The West African craton*. BRGM. ed, Memory of BRGM. Paris.
12. Béziat, D., Dubois, M., Debat, P., Nikiéma, S., Salvi, S., Tollon, F. (2008). Gold metallogeny in the Birimian craton of Burkina Faso (West Africa). *Journal of African Earth Sciences* 50, 215–233. <https://doi.org/10.1016/j.jafrearsci.2007.09.017>
13. Boateng, D.Y.A., Morufdeen, A.A., Jnr, E.M.O., Ntori, C. (2018). Hydrothermal Alteration Mapping, Using the Crosta Technique: Case Study of the Kibi Goldfields Osino Concession, Ghana. *IJESG*, 8(12), 8.
14. Castaing, C., Le Métour, J., Billa, M. (2003). Explanatory note for the 1:1,000,000 geological and mining map of Burkina Faso.
15. Clark, R.N. (1999). USGS Spectroscopy Lab: Spectroscopy of Rocks and Minerals, and Principles of Spectroscopy, 293p.

16. Dabiri, Z., Lang, S. (2018). Comparison of Independent Component Analysis, Principal Component Analysis, and Minimum Noise Fraction Transformation for Tree Species Classification Using APEX Hyperspectral Imagery, 26.
17. Daoud, A.M.A., Shebl, A., Abdelkader, M.M., Mohieldain, A.A., Csámer, A., Satti, A.M.N., Rózsa, P. (2025). Remote sensing and gravity investigations for barite detection in Neoproterozoic rocks in the Ariab area, Red Sea Hills, Sudan. *Remote Sensing Applications: Society and Environment* 37, 101416. <https://doi.org/10.1016/j.rsase.2024.101416>
18. Dupuis, D., Pons, J., E Prost, A. (1991). Pluton emplacement and characterization of birimian deformation in western Niger. *C. R. Acad. Sci. Paris* 312, 769–776.
19. Eteh, D.R., Francis, E.E., Ajoko, I.T. (2021). Gis and remote sensing technology in evaluation of geostatistical heavy metals soil for environmental quality in yenagoa metropolis, Bayelsa state Nigeria. *J. Appl. Sci. Envir. Stud.* 4(1), 286-307.
20. Elsaid M. (2014). Mapping of Limonite minerals (Ferrugination), Ferrumagnesians and OH-Bearing (Clays, Micas) & carbonate minerals using band rationing of Landsat 8 OLI (Surface Reflectance) bands.
21. Frutuoso, R. (2015). Mapping hydrothermal gold mineralization using Landsat 8 data. A case of study in Chaves license, Portugal. MEDGOLD Resources Inc, 85.
22. Gabr, S., Ghulam, A., Kusky, T. (2010). Detecting areas of high-potential gold mineralization using ASTER data. *Ore Geology Reviews* 38 (2010) 59–69. doi:10.1016/j.oregeorev.2010.05.007
23. Ge, W., Cheng, Q., Jing, L., Wang, F., Zhao, M., Ding, H. (2020). Assessment of the Capability of Sentinel-2 Imagery for Iron-Bearing Minerals Mapping: A Case Study in the Cuprite Area, Nevada. *Remote Sensing* 12, 3028. <https://doi.org/10.3390/rs12183028>
24. Ghrefat, H., Awawdeh, M., Howari, F., Al-Rawabdeh, A. (2023). Chapter 12 - Mineral exploration using multispectral and hyperspectral remote sensing data, in: Stathopoulos, N., Tsatsaris, A., Kalogeropoulos, K. (Eds.), *Geoinformatics for Geosciences, Earth Observation*. Elsevier, pp. 197–222. <https://doi.org/10.1016/B978-0-323-98983-1.00013-2>
25. Han, T., Nelson, J. (2014). Mapping hydrothermally altered rocks with Landsat 8 imagery: A case study in the KSM and Snowfield zones, northwestern British Columbia 10.
26. Ibrahim, M., Kotelnikov, A., Podolko, P., Kotelnikova, E. (2021). Remote sensing data for Geological mapping and gold prospecting of Inteet area, northern Sudan. *E3S Web Conf.* 258, 03009. <https://doi.org/10.1051/e3sconf/202125803009>
27. Kamau, M., Hecker, C., Lievens, C. (2020). Use of Short-Wave Infrared Reflectance (SWIR) Spectroscopy to Characterize Hydrothermal Alteration Minerals in Olkaria Geothermal System, Kenya. *PROCEEDINGS, 45th Workshop on Geothermal Reservoir Engineering Stanford University, Stanford, California, February 10-12, 2020 SGP-TR-216*, 15p.
28. Khidir, S.O.E., Babikir, I.A.A. (2013). Digital image processing and geospatial analysis of landsat 7 ETM+ for mineral exploration, Abidiya area, North Sudan. *International Journal of Geomatics and Geosciences* 3, 14.
29. Klockner (1995). Gold research in Liptako. Ministry of Mines and Energy, Niamey. Final report n° 6500-11-40-026, 162p.
30. Kokaly, R.F., Clark, R.N., Swayze, G.A., Livo, K.E., Hoefen, T.M., Pearson, N.C., Wise, R.A., Benzel, W.M., Lowers, H.A., Driscoll, R.L., Klein, A.J. (2017). USGS Spectral Library Version 7 (Data Series 1035), Data Series. U.S. Geological Survey. 61p. <https://doi.org/10.3133/ds1035>.
31. Kruse, F.A., Hauff, P.L. (1990). Remote sensing clay mineral investigations for geologic applications using visible/infrared imaging spectroscopy. *Sci. Géol., Mém.*, 89, p. 43-51.
32. Kujjo, C., Liang, L., Ravat, D. (2018). Mapping hydrothermal alteration zones in the didinga hills, south sudan. *International Journal of Remote Sensing* 7(2), 9.
33. Kujjo, C.P. (2010). Application of Remote Sensing for Gold Exploration in the Nuba Mountains, Sudan. Master of Science, College of Bowling Green, State University. 110p.
34. Labdaoui, B., Benali, H., Boughacha, A., Moussaoui, K. (2023). Mapping hydrothermal alterations and lineaments associated with epithermal and massive sulphides deposits of Tifraouine (northwest Algerian coast): Use of Landsat 8 OLI data and remote sensing. *Rev.Soc.Geo.Esp* 36, 3–15. <https://doi.org/10.55407/rsge.96703>
35. Long, D.T., Fegan, N.E., McKee, J.D., Lyons, W.B., Hines, M.E., Macumber, P.G. (1992). Formation of alunite, jarosite and hydrous iron oxides in a hypersaline system: Lake Tyrrell, Victoria, Australia. *Chemical Geology* 96, 183–202. [https://doi.org/10.1016/0009-2541\(92\)90128-R](https://doi.org/10.1016/0009-2541(92)90128-R)
36. Machens, E. (1973). Contribution to the study of crystalline basement formations and sedimentary cover in the western Niger Republic. *Memory of BRGM No. 82*, 158p.
37. Machens, E. (1967). Geological map of western Niger. *Memory of BRGM*.
38. Markwitz, V., Hein, K.A.A., Jessell, M.W., Miller, J. (2016). Metallogenic portfolio of the West Africa craton. *Ore Geology Reviews* 78, 558–563. <https://doi.org/10.1016/j.oregeorev.2015.10.024>
39. Markwitz, V., Hein, K.A.A., Miller, J. (2015). Compilation of West African mineral deposits: Spatial distribution and mineral endowment. *Precambrian Research* 274, 61–81. <https://doi.org/10.1016/j.precamres.2015.05.028>

40. Mars, J.C., Rowan, L.C. (2006). Regional mapping of phyllic- and argillic-altered rocks in the Zagros magmatic arc, Iran, using Advanced Spaceborne Thermal Emission and Reflection Radiometer (ASTER) data and logical operator algorithms. *Geosphere* v. 2; no. 3; p. 161–186; doi: 10.1130/GES00044.1
41. Massironi, M., Bertoldi, L., Calafa, P., Visonà, D., Bistacchi, A., Giardino, C., Schiavo, A. (2008). Interpretation and processing of ASTER data for geological mapping and granitoids detection in the Saghro massif (eastern Anti-Atlas, Morocco). *Geosphere* 4, 736. <https://doi.org/10.1130/GES00161.1>
42. Milési, J.-P., Feybesse, J.-L., Ledru, P., Dommangeat, A., Ouedraogo, M.-F., Marcoux, E., Prost, A., Vinchon, C., Sylvain, J.-P., Johan, V., Tegye, M., Calvez, J.-Y., Lagny, P. (1989). Gold mineralization in West Africa. Their relationship with lithostructural evolution in the Lower Proterozoic. *Chron. rech. min.* 497, 3–98.
43. Milési, J.-P., Feybesse, J.-L., Pinna, P., Deschamps, Y., Kampunzu, H., Muhonogo, S., Lescuyer, J.-L., Toteu, S. (2004). *Geology and main deposits of Africa, scale 1/10,000,000*.
44. Mwaniki, M.W., Moeller, M.S., Schellmann, G. (2015). A comparison of Landsat 8 (OLI) and Landsat 7 (ETM+) in mapping geology and visualising lineaments: A case study of central region Kenya. *Int. Arch. Photogramm. Remote Sens. Spatial Inf. Sci.* XL-7/W3, 897–903. <https://doi.org/10.5194/isprsarchives-XL-7-W3-897-2015>
45. Osinowo, O.O., Gomy, A., Isseini, M. (2021). Mapping hydrothermal alteration mineral deposits from Landsat 8 satellite data in Pala, Mayo Kebbi Region, Southwestern Chad. *Scientific African* 11, e00687. <https://doi.org/10.1016/j.sciaf.2020.e00687>
46. Ourhzi, Z., Algouti, A., Algouti, A., Hadach, F. (2019). Lithological mapping using landsat 8 oli and aster multispectral data in imini-ounilla district south high atlas of marrakech. *Int. Arch. Photogramm. Remote Sens. Spatial Inf. Sci.* XLII-2/W13, 1255–1262. <https://doi.org/10.5194/isprs-archives-XLII-2-W13-1255-2019>
47. Payamani, A., Babaei, B., Dehghan, S., AsadiHarouni, H. (2020). Applying various satellite image processing methods on Aster and Landsat ETM+ data to identify and separate the alteration zones around gold mine of Akhtarchi, Khomein, Iran. *Nexo Revista Científica* 33, 490–510. <https://doi.org/10.5377/nexo.v33i02.10787>
48. Pons, J., Barbey, P., Dupuis, D., Léger, J.M. (1995). Mechanisms of pluton emplacement and structural evolution of a 2.1 Ga juvenile continental crust: the Birimian of southwestern Niger. *Precambrian Research* 70, 281–301. [https://doi.org/10.1016/0301-9268\(94\)00048-V](https://doi.org/10.1016/0301-9268(94)00048-V)
49. Poormirzaee, R., Oskouei, M.M. (2010). Use of spectral analysis for detection of alterations in ETM data, Yazd, Iran. *Appl Geomat* 2, 147–154. <https://doi.org/10.1007/s12518-010-0027-8>
50. Poulin, R., Kima, A., Savard, R. (1987). 1986-87 prospecting campaign at Koma Bangou, Niger. Ministry of Mines and Energy, ONAREM. Tome 1 (No. 227), 209p.
51. Pour, A.B., Hashim, M. (2015). Hydrothermal alteration mapping from Landsat-8 data, Sar Cheshmeh copper mining district, south-eastern Islamic Republic of Iran. *Journal of Taibah University for Science* 9, 155–166. <https://doi.org/10.1016/j.jtusci.2014.11.008>
52. Pour, A.B., Hashim, M. (2011). Application of advanced spaceborne thermal emission and reflection radiometer (ASTER) data in geological mapping. *International Journal of the Physical Sciences* 6, 7657–7668.
53. Pour, A.B., Park, T.-Y.S., Park, Y., Hong, J.K., Muslim, A.M., Läuffer, A., Crispini, L., Pradhan, B., Zoheir, B., Rahmani, O., Hashim, M., Hossain, M.S. (2019). Landsat-8, Advanced Spaceborne Thermal Emission and Reflection Radiometer, and WorldView-3 Multispectral Satellite Imagery for Prospecting Copper-Gold Mineralization in the Northeastern Inglefield Mobile Belt (IMB), Northwest Greenland 39. *Remote Sens.* 2019, 11, 2430; doi:10.3390/rs11202430
54. Rajesh, H.M. (2004). Application of remote sensing and GIS in mineral resource mapping-An overview. *Journal of Mineralogical and Petrological Sciences* 99, 83–103. <https://doi.org/10.2465/jmps.99.83>
55. Sabins, F.F. (1999). Remote sensing for mineral exploration. *Ore Geology Reviews* 14, 157–183. [https://doi.org/10.1016/S0169-1368\(99\)00007-4](https://doi.org/10.1016/S0169-1368(99)00007-4)
56. Saint-Martin, M. (1999). Liptako Mineral Exploration Project (Final Report). Ministry of Mines and Energy, 457p.
57. Sekandari, M., Masoumi, I., Beiranvand Pour, A., M Muslim, A., Rahmani, O., Hashim, M., Zoheir, B., Pradhan, B., Misra, A., Aminpour, S.M. (2020). Application of Landsat-8, Sentinel-2, ASTER and WorldView-3 Spectral Imagery for Exploration of Carbonate-Hosted Pb-Zn Deposits in the Central Iranian Terrane (CIT). *Remote Sensing* 12, 1239. <https://doi.org/10.3390/rs12081239>
58. Sgavetti, M., Pompilio, L., Meli, S. (2006). Reflectance spectroscopy (0.3–2.5 μm) at various scales for bulk-rock identification. *Geosphere* 2, 142. <https://doi.org/10.1130/GES00039.1>
59. Shawky, M.M., El-Arafy, R.A., El Zalaky, M.A., Elarif, T. (2019). Validating (MNF) transform to determine the least inherent dimensionality of ASTER image data of some uranium localities at Central Eastern Desert, Egypt. *Journal of African Earth Sciences* 149, 441–450. <https://doi.org/10.1016/j.jafrearsci.2018.08.022>
60. Sheikhrhimi, A., Pour, A.B., Pradhan, B., Zoheir, B. (2019). Mapping hydrothermal alteration zones and lineaments associated with orogenic gold mineralization using ASTER data: A case study from the Sanandaj-Sirjan Zone, Iran. *Advances in Space Research* 63, 3315–3332. <https://doi.org/10.1016/j.asr.2019.01.035>
61. Soumaila, A. (2000). Structural, petrographic and geochemical study of the Diagorou-DarbaniLiptakobirimian belt, western Niger (West Africa). PhD thesis, Université de Franche-comté, France, 260p.

62. Soumaila, A., Henry, P., Rossy, M. (2004). Setting context of the basic rocks of the Diagorou-Darbani Birimian greenstone belt (Liptako, Niger, West Africa): oceanic plateau or arc environment/ oceanic back-arc basin. *Comptes Rendus Geoscience* 336, 1137–1147. <https://doi.org/10.1016/j.crte.2004.03.008>
63. St-Julien, P. (1992). Preliminary structural study of the Kourki, Dounga, Kosso and Borobon showings in the Gorouol belt (Liptako). ACDI Report N° 700/10417. 34p.
64. Traore, M., Can, T., Tekin, S. (2020). Discrimination of Iron Deposits Using Feature Oriented Principal Component Selection and Band Ratio Methods: Eastern Taurus/Turkey. *IJEGEO* 7(2), 12.
65. Xu, K., Wang, X., Kong, C., Feng, R., Liu, G., Wu, C. (2019). Identification of Hydrothermal Alteration Minerals for Exploring Gold Deposits Based on SVM and PCA Using ASTER Data: A Case Study of Gulong. *Remote Sensing* 11, 3003. <https://doi.org/10.3390/rs11243003>

UNDER PEER REVIEW